Electronic response of C_{60} in slow collisions with highly charged ions

H. Cederquist, A. Fardi, K. Haghighat, A. Langereis, H. T. Schmidt, and S. H. Schwartz
Atomic Physics, Stockholm University, Frescativ. 24, S-104 05 Stockholm, Sweden

J. C. Levin and I. A. Sellin
Department of Physics and Astronomy, University of Tennessee, Knoxville, Tennessee 37996-1200

H. Lebius and B. Huber
Département de Recherche Fondamentale sur la Matière Condensée/ S12A CEA-Grenoble, 17 rue des Martyrs, F- 30854, Grenoble Cedex 9, France

M. O. Larsson* and P. Hvelplund
Institute of Physics, University of Aarhus, DK-8000 Aarhus C, Denmark
(Received 14 May 1999; published 12 January 2000)

We present measurements of projectile angular differential cross sections, $d\sigma/d\theta$, and mean projectile energy gain or loss, ΔE_{mean}, as functions of the number s of electrons stabilized on the projectile in 16- and 26.4-keV $Ar^{8+}+C_{60}\rightarrow Ar^{(8-s)+}+C_{60}{}^{r+}+(r-s)e^-$ collisions. These results are discussed in view of two models of the electronic response of C_{60}. In the infinitely conducting sphere model the charge mobility is sufficiently high in order to average out all effects of localization of individual charge carriers. In the movable-hole model ''positive holes'' are assumed to be localized as point charges in their equilibrium positions on the ''molecular surface'' within the times (down to 10^{-16} s) between sequential over-the-barrier electron transfers. The two sets of predictions for θ are close for $r\leqslant 8$, and for $r\leqslant 5$ they are also in agreement with experimental results indicating ultrafast electronic response of ionized C_{60}. For $r>5$, both models underestimate θ and therefore we have developed Monte Carlo calculations for close collisions with individual carbon atoms in C_{60}. The energy gain first increases with s, has a flat maximum around $s=4$ and yields mean energy loss $\Delta E_{mean}=-20\pm 5$ eV for $s=7$. The measured fragmentation spectra $\theta(s)$ and $\Delta E_{mean}(s)$ may be partially rationalized by combining each of the two smooth-sphere models with the Monte Carlo calculations for close collisions.

PACS number(s): 34.70.+e, 34.50. Fa, 36.40.−c

I. INTRODUCTION

The issue about the electric response of a C_{60} molecule interacting with a slow highly charged ion relates directly to the ideas of using fullerenes and nanowires as building blocks for novel nanoelectronics. It is well known that the electrical properties of fullerene materials depend on the details of the geometrical and molecular structure and, in the case of fullerite, on the doping with foreign atoms. For such different parameters fullerene materials may be isolating, semiconducting, conducting, or even superconducting at fairly high critical temperatures [1]. In fullerite, the C_{60} molecules form a very loosely bound van der Waals crystal and the individual molecules are only slightly perturbed by their neighbors. The low conductivity of the crystal may thus be understood in terms of the completely filled highest occupied molecular orbital (HOMO) level of C_{60}. This situation changes drastically when the crystal is doped with alkali-metal atoms in exohedral and endohedral positions. Electrons are then donated to the lowest unoccupied molecular orbital band through charge transfer and the conductivity of the crystal may be increased drastically depending on the number of donating atoms per C_{60} molecule [1].

In the present work, we instead remove electrons from the HOMO level of individual C_{60} molecules in gas phase and, in a sense, one would expect the ''electrical conductivity'' of the molecule to be affected by the number of electrons in the outermost molecular orbital. In the present experiments, one or several electrons are transferred from C_{60} to slow Ar^{8+} projectile ions in single collisions at 16 and 26.4 keV:

$$Ar^{8+}+C_{60}\rightarrow Ar^{(8-s)+}+C_{60}{}^{r+}+(r-s)e^-. \qquad (1)$$

The number of electrons stabilized on the projectile ranges from $s=1$ to $s=8$ and the total collision time during which r electrons are removed from the target is about 10 fs.

We have measured projectile angular differential cross sections $d\sigma/d\theta$, mean projectile energy gain or loss ΔE_{mean}, and fragmentation patterns as functions of s. These results will be discussed within two different classical over-the-barrier models in which the electrons are transferred sequentially with time separations of 0.1–1 fs. In the infinitely conducting sphere (ICS) model, the electronic response time is infinitely short, i.e., the electronic motion averages out all effects of localization of individual charge carriers. In the model with r positive and localized holes moving on ''the surface'' of $C_{60}{}^{r+}$ the charge mobility can be controlled. This is done by adjusting the time required to reach new equilibrium charge configurations after each (sequential)

*Present address: Uppsala University, Uppsala, Sweden.

 ©2000 The American Physical Society

electron transfer. A response time of 10^{-16} s in the movable hole (MH) model is found to yield results in agreement with experiments and the ICS model for small and moderate $r(r \leqslant 5)$.

The first investigation of the interaction between highly charged ions and C_{60} was performed by Walch *et al.* [2] for 80-keV $Ar^{8+}+C_{60}$ collisions. It then immediately became evident that slow highly charged ions are very efficient means for cold multiple ionization of fullerenes. The cross sections for producing stable, or at least metastable, and intact C_{60}^{r+} with r ranging up to six were found to be large [2]. Two years later this result was underscored by Jin *et al.* [3] who measured intact C_{60}^{9+} produced by slow Bi^{44+} impact. Very recently, Huber and coworkers [4] were able to show that C_{60}^{10+} produced by Xe^{25+} impact are metastable with lifetimes in the μs range. A further very intriguing recent result is that r may exceed the projectile charge by a factor of 3 for $q>30$ in slow fragmenting Xe^{q+}-C_{60} collisions [5].

Thumm *et al.* [6] used the dynamical classical over-the-barrier model for a metal (infinitely conducting) sphere to calculate translational energy gain mainly in good agreement with measurements by Selberg *et al.* [7]. This concept has also been used to successfully account for critical electron transfer distances [8], the polarizability of C_{60} [9], surface plasmon excitation in collisions with electrons [10], the sequence of ionization potentials [11], and radiative cooling of hot C_{60}^{-} [12]. A general model, in which the C_{60} molecule is treated as a dielectric sphere, has been developed by Bárány and Setterlind [13]. This model was later used in order to calculate translational energy gain spectra for relative dielectric constants between $\epsilon_r=1$ (insulating sphere) and $\epsilon_r=\infty$ (infinitely conducting sphere) [14].

In 1995, Shen *et al.* [15] measured large cross sections for nonfragmenting single, and double-electron capture in fullerene-fullerene collisions (C_{60}^{q+}-C_{60}). Electrons may thus obviously be transferred at distances large enough to avoid strong direct interactions between the molecular cages. Shen *et al.* [15] invoked the model with movable and localized charges to rationalize their results. This model has also been used in order to account for charge-insensitive electron-capture cross sections in near thermal collisions between multiply charged fullerenes and various atoms [16,17]. Further, Sheier, Dünser and Märk [18] used a similar idea in order to explain the weak q dependence of the critical C_{58}^{q+}-C_2 distances for electron transfer in the auto charge-transfer fragmentation process $C_{60}^{q+}\rightarrow C_{58}^{(q-1)+}+C_2^{+}$.

The infinitely conducting-sphere and the movable-hole models have thus both been successfully used to account for various experimental observations. In the present study we find, nevertheless, that the two seemingly very different models yield similar predictions for $\theta(r)$ and $\Delta E_{mean}(r)$. For small and moderate values of r both models are in good agreement with the experimental results, while their values for θ at large r lie far below the measurements. These discrepancies are, at least partly, accounted for by including the effects of close collisions, i.e., we take the scattering on individual Carbon atoms in the C_{60} molecule into account.

The experimental techniques employed to measure $d\sigma/d\theta$, ΔE_{mean} and absolute cross sections σ_s as functions of s are described in Sec. II A. In Sec. II B we account for the methods to measure the total (integrated over s and ΔE) and the s-selective fragmentation spectra. In Sec. III A we give a detailed account for the present version of the infinitely conducting-sphere model, which is similar to but simpler than the one used by Thumm *et al.* [6]. The details of the model with movable and localized charges on a smooth sphere are presented in Sec. III B, while the Monte Carlo calculations for close collisions are described in Sec. III C. The experimental results for σ_s, $d\sigma/d\theta(s)$, $\Delta E_{mean}(s)$, and the fragmentation are discussed in view of the ICS (infinitely conducting sphere) and the MH (movable hole) models, with and without the contributions from close collisions, in Secs. IV A-IV C. Finally in Sec. IV D, we discuss fragmentation in view of the statistical model by Campbell, Raz, and Levine [19] and recent results by Schlathölter *et al.* [20].

II. EXPERIMENTAL TECHNIQUES AND PROCEDURES

A. Measurements of $d\sigma/d\theta$ and ΔE

The Cryogenic Electron Beam Ion Source at the Manne Siegbahn Laboratory in Stockholm was used to provide a beam of highly charged Ar ions. A double-focusing analyzing magnet separated its Ar^{8+}-ion component at an energy of 26.4 keV. The Ar^{8+}-ion beam was collimated by two sets of apertures to an angular definition of $\delta\theta=\pm 0.015\,^\circ$ before it entered a C_{60}-cell of 30 mm length and entrance and exit apertures of 1.0 and 1.5 mm, respectively. This yielded an overall measured angular resolution of $\pm 0.02\,^\circ$. Care was taken to operate the cell in a temperature interval (410–420 °C) giving a total charge-exchange yield below 10%, which made corrections for double and background collisions small but not insignificant. The charge exchange with the background gas was measured at a cell temperature of 300 °C.

In order to be able to measure the angular and energy distributions resulting from the various electron transfer processes, three different analyzing systems were used (see Fig. 1). Each system *A*-*C* was preceded by the same 300-mm-long, field-free, drift region after the cell. System *A* consisted of a 180° cylindrical energy analyzer of radius 150 mm followed by a two-dimensional position-sensitive detector. The angular acceptance of system *A* was $\Delta\theta_A=\pm 0.5\,^\circ$ and the cylindrical analyzer is only focusing the beam in one direction.

From the resulting image on the detector we extracted $d\sigma/d\theta(s)$ for s ranging from one to seven, i.e., for processes in which the incident Ar^{8+} ions stabilize up to $s=7$ electrons for (at least) the duration of their passage through the energy analyzer (which takes about 1 μs). The focusing of the cylindrical analyzer distorts the images on the detector rather strongly as can be seen in the upper right part of Fig. 1. The angular differential cross sections could, however, be obtained by means of off-line sorting of the detector image part inside a bow-tie aperture (defined by γ in Fig. 1) oriented along the nonfocusing direction. Due to the strong distortion, it was necessary to keep the opening angle γ of the

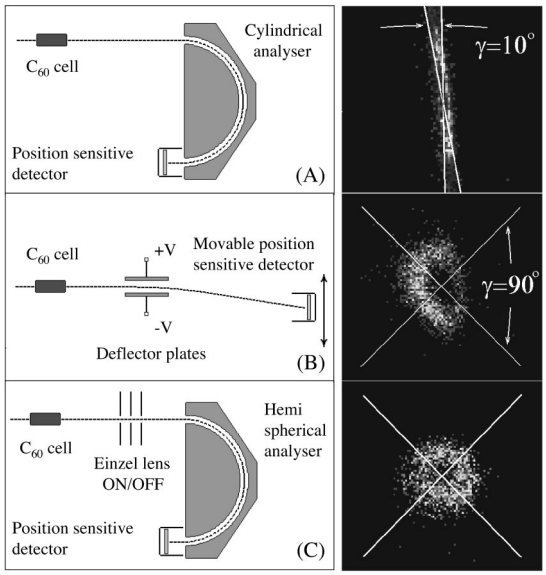

FIG. 1. The three different experimental techniques *A*, *B*, and *C* used to measure $d\sigma/d\theta$ and mean values of energy gain/loss as functions of s in Ar^{8+}-$C_{60} \rightarrow Ar^{(8-s)+}$- . . . collisions at 26.4 keV. The images on the detector for the $s=6$ process are shown to the far right, where the bow-tie apertures, with opening angles γ, indicate the areas used for extraction of $d\sigma/d\theta$. The distances from the center of the bow tie are used to calculate θ for each event taking the focusing of the respective analyzing system into account. The detector image for system *C* is shown with the einzel lens off, while this lens was turned on for the ΔE measurements.

bow-tie small ($\gamma=10°$), which limited the statistical quality of the resulting $d\sigma/d\theta$ spectra. In order to cope with this problem and to be able to measure the angular distribution also for neutralizing collisions ($s=8$) we also used system *B*. This system consisted of a set of 100-mm-long straight deflection plates followed by a drift region of length 540 mm terminated by a movable position-sensitive detector. The different outgoing final projectile charge states, $q'=8-s$, were dispersed on the detector by means of different deflection voltages making the $Ar^{q'+}$-ion beam of interest deflect about 10°. For the neutralized projectiles (outgoing Ar atoms), the detector was placed in the straight forward direction and the charged particles were deflected away by a high voltage on the plates. The angular acceptance of system *B* was $\Delta\theta_B = \pm 1.0°$.

Finally system *C* was used in order to measure modest resolution translational energy-gain distributions for processes with up to seven stabilized electrons ($s=1-7$). System *C* was similar to *A* except that the cylindrical analyzer was replaced by a double-focusing hemispherical one with the same radius (150 mm). An einzel lens was introduced in front of the analyzer in order to focus the beam to a small spot on the detector. Thus, the kinetic energy distributions of the seven outgoing $Ar^{q'+}$-ion beams could be better resolved.

B. Measurements of fragmentation spectra

The time-of-flight spectra of fragmenting and intact C_{60}^{r+} recoil ions were measured in coincidence with the outgoing projectile charge state ($q'=8-s$) for 16-keV Ar^{8+}-C_{60} collisions. These measurements were performed at CEA-Grenoble in France and the technique also allowed for energy-gain selective recording of the fragment spectra for various values of *s*. Measurements of the latter kind are reported in a separate paper (Opitz *et al.* [21]). The data discussed here, however, are obtained by (i) averaging over all values of *s* and energy gain or loss and (ii) by averaging over the ΔE distributions for individual values of *s* ($s=1$, 2, 3, 4, and 6). For a schematic of the setup and details of the experimental technique we refer to Opitz *et al.* [21] and here we will only give a brief description of the most important parts.

A beam of 16-keV Ar^{8+} is provided by a 14-GHz ECR source and a double-focusing bending magnet. This beam was then passed through an energy monochromator consisting of two hemispherical electrostatic analyzers, lenses, and slits by which the incident Ar^{8+}-ion beam energy was defined to about $\delta E = \pm 10$ eV. The beam then crosses with an effusive C_{60} jet and the point of intersection is situated in the extraction region of a 250-mm-long time-of-flight mass spectrometer. This spectrometer is terminated by a multichannel plate (MCP) detector at which the intact recoils or fragments have energies of 6-keV times their charge. The angular, energy, and charge-state distributions of the scattered projectiles are analyzed by means of a set of two hemispherical analyzers in series that may be rotated around the scattering center. The data that will be shown here are all obtained in the forward direction with the angular acceptance $\Delta\theta = \pm 0.3°$.

In method (i) the Ar^{8+}-ion beam and the extraction voltage were pulsed in order to obtain the total fragmentation spectra. The start signal for the time of flight was provided by the extraction pulse and care was taken to allow the projectile beam to pass through the extraction region before the extraction pulse was switched on. The rates of detection for the various intact ions and fragments were investigated as functions of the time between the passage of the projectile ions and the extraction pulse, the extraction, and drift voltages in the time-of-flight spectrometer and the front bias of the MCP detector. Saturations of the detection efficiencies as functions of all these parameters were found, except for C_2^+ which is known to have a high kinetic energy from the fragmentation process [18]. The data acquisition system allowed for multihit registration of fragments and therefore we measure the true relative production cross sections for the individual fragments and the intact molecules. The statistics of the different multihit events may of course be used to derive more information on the charge-exchange and fragmentation processes. This will, however, be discussed in a separate paper (Opitz *et al.* [22]).

The fragment spectra for individual values of the number of electrons stabilized by the Ar^{8+}-ion projectile after the collision are obtained with a different technique, method (ii). The Ar^{8+}-ion beam is now continuous and the recoil ion-extraction voltage is fixed. The analyzer voltages are scanned many times over the complete ΔE distributions for the different values of *s* while the time-of-flight spectra are recorded.

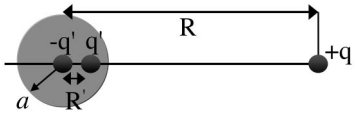

FIG. 2. An ion of charge q at a distance R outside an infinitely conducting neutral sphere of radius a. The position of the image charge $q'=-aq/R$ is given by $R'=a^2/R$. An equally large positive charge $-q'=+aq/R$ is positioned in the center of the sphere (cf. text).

III. MODELS OF HCI-C_{60} INTERACTIONS

A. Highly charged ions scattering on an infinitely conducting sphere

In this first model, we follow Walch *et al.* [2,23], Thumm [8], Thumm *et al.* [6], and Bárány and Setterlind [13]. We assume that C_{60} is an infinitely conducting sphere with its radius $a=8.2a_0$ given by the consensus value for the polarizability of the C_{60} molecule ($543a_0^3$) from Scheidermann *et al.* [9]. When an ion of charge q is brought near the sphere, the conduction electrons are attracted by the ion and an inhomogenous surface-charge distribution is created. The electric field inside the sphere is zero (it is infinitely conducting) and on the outside it can be calculated easily by means of the method of electrostatic images [24]. The crucial point here is that the sphere surface must remain an equipotential surface for all (sufficiently large) distances R between the ion and the center of the sphere. This criterion leads to the unique solution for the magnitude $q'=-qa/R$ and the position $R'=a^2/R$ of the image charge (see Fig. 2).

Further, in order to conserve the total charge an equally large positive charge $-q'=+qa/R$ must be placed in its center (the only position compatible with the equipotential surface condition).

The electric field from the infinitely conducting sphere, with its inhomogenous surface-charge distribution, at the position of the ion is exactly

$$E(R)=\frac{q'}{(R-R')^2}-\frac{q'}{R^2}, \tag{2}$$

and the force on the ion thus becomes

$$F_q(R)=qE(R)=\frac{aq^2}{R^3}-\frac{aq^2R}{(R^2-a^2)^2}. \tag{3}$$

$F_q(R)$ is always attractive and we calculate the work required to move q from $R(>a)$ to infinity as

$$W_q=-\int_R^\infty F_q dR=-\frac{1}{2}\left(\frac{aq^2}{R^2}-\frac{aq^2}{R^2-a^2}\right). \tag{4}$$

Thus, the electric potential at the position of the ion is given by $U_q=W_q/q$. For large R, Eq. (4) can be approximated by $W_q\approx -a^3q^2/2R^4$ where $\alpha=a^3$ is the static dipole polarizability of the sphere.

We further assume that the work function of the neutral infinitely conducting sphere is equal to the first ionization potential of C_{60}, denoted by I_1. In the presence of the ion, the energy required to ionize the sphere is shifted according to

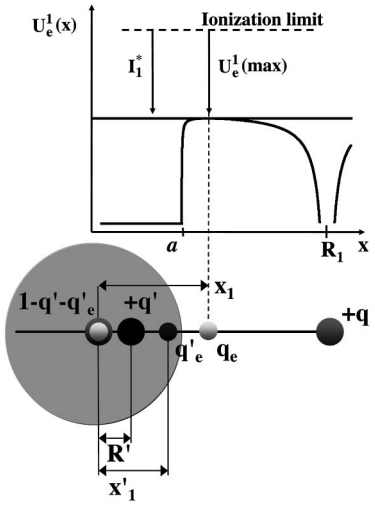

FIG. 3. The potential energy seen by the active electron at the first critical distance R_1 for electron transfer. The electron is at the position $x=x_1$ where the potential $U_e^1(x)$ has its maximum $U_e^1(max)$. The potential $U_e^1(x)$ is given by q and its image charge q', the net charge of the infinitely conducting sphere $(+1)$ and the active electrons self-image potential. The image charges due to the ion and the electron are $q'=-aq/R_1$ and $q'_e=a/x_1$ at the positions $R'=a^2/R_1$ and $x'_1=a^2/x_1$, respectively. The central charge is $1-q'-q'_e=1+aq/R_1-a/x_1$ and $q_e=-1$ in atomic units.

$$I_1^*=I_1+q/R. \tag{5}$$

This is due to the shift in the electric potential ϕ, which is common for all points belonging to the sphere. We can, for example, calculate ϕ for the point on the surface closest to the ion as

$$\phi=q/(R-a)+q'/(a-R')-q'/a=q/R. \tag{6}$$

The critical distance $R=R_1$ at which the first electron may leave the sphere is assumed to be given by the classical over-the-barrier criterion $U_e^1(max)=I_1^*$, where $U_e^1(max)$ is the maximum of the potential U_e^1 seen by the first active electron when it moves towards the projectile. This potential can be expressed in terms of the electrons interaction with the projectile ion and its induced charges (q' and $-q'$), the net $+1$ charge of the sphere (represented by a point charge in its center) and the electrons self-induced image. We thus have

$$U_e^1=-\frac{q}{R-x}-\frac{q'}{x-R'}+\frac{q'-1}{x}+\frac{1}{2}\left(\frac{a}{x^2}-\frac{a}{x^2-a^2}\right), \tag{7}$$

where x is the position of the electron with respect to the center of the sphere. The case with the electron at $x=x_1$, i.e., at the top of the barrier is shown in Fig. 3

When the first electron is transferred to the projectile, the force on the ion changes abruptly according to the new charge distribution. We assume that the initial projectile charge q is fully screened by the electrons transferred from

the infinitely conducting sphere. Thus, we introduce R-dependent projectile and target charges according to

$$q_p(R)=q-q_t(R), \tag{8}$$

where $q_t(R)$ only can take integer values r. This is in accordance with the assumptions made in over-the-barrier models for ion-atom [25] and ion-surface collisions [26–28]. In particular, it has been shown through measurements of the image charge acceleration for highly charged ions interacting with a metal surface [29] that the projectile is neutralized in a step-wise manner [28,30] consistent with Eq. (8).

In analogy with Eq. (5), the energy required to ionize an $(r-1)$-times charged infinitely conducting sphere is

$$I_r^*=I_r+(q-r+1)/R, \tag{9}$$

in the presence of the projectile, of charge $q_p=(q\text{-}r+1)$. Accordingly, the Stark-shifted target level, I_r^*, has to reach the top of the potential barrier created by

$$U_e^r=-\frac{q-r+1}{R-x}+\frac{a(q-r+1)}{R(x-R')}-\frac{a(q-r+1)}{Rx}$$
$$-\frac{r}{x}+\frac{1}{2}\left(\frac{a}{x^2}-\frac{a}{x^2-a^2}\right) \tag{10}$$

for the rth electron to be able to move to the projectile. The sequence of ionization potentials for an isolated infinitely conducting sphere of radius a is given by

$$I_r=(r+1)/a, \tag{11}$$

which for $a=8.2a_0$ gives $I_r=3.32(r+1)$ eV in fair agreement with experimental ionization potentials [31,32]. In the present calculation we have, however, chosen to follow Walch *et al.* [23] and used the slightly different expression $I_r=3.85+3.39r$, which they [23] in turn based on the Dirac-Fock-Slater calculations by Bastug *et al.* [33].

After transfer of the rth active electron and for values of R such that $R_{r+1}<R<R_r$, the force on the ion, now of charge $q_p=q-r$, is

$$F_{q-r}=\frac{(q-r)r}{R^2}+\frac{a(q-r)^2}{R^3}-\frac{a(q-r)^2R}{(R^2-a^2)^2}. \tag{12}$$

We arrive at a series of eight sequential electron transfers for the incident projectile charge $q=8$ by setting $U_e^r(max)=I_r^*$ for $r=1$ through $r=8$. These distances all lie well outside the radius of the sphere ($a=8.2a_0$) and the radius of the C_{60} cage of carbon nuclei ($a_{cage}=6.7a_0$). The first electron transfers at $R_1=26.5a_0$, the second at $R_2=21.4a_0$, and the eighth at $R_8=10.6a_0$. The projectile may thus be fully neutralized in a single collision with an infinitely conducting sphere even though full screening of the projectile charge is assumed. Note that the eighth electron is transferred at a distance of about $4a_0$ above the C_{60} cage.

In the Monte Carlo calculations based on the infinitely conducting-sphere model, the impact parameters with respect to the center of the sphere $b_{C_{60}}$ (cf. Fig. 4) are randomly selected between preset minimum and maximum values.

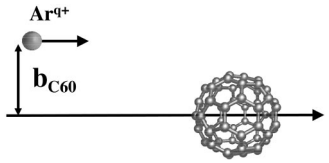

FIG. 4. Definition of the impact parameter with respect to the center of C_{60}: $b_{C_{60}}$.

For each value of $b_{C_{60}}$, we follow the ion trajectory and integrate the dynamically changing force taking the R_r sequence of electron transfers into account. We calculate the projectile scattering angle θ from the momentum transfer in the direction perpendicular to the initial velocity vector. The momentum transfer in the longitudinal direction gives the Q value of the reaction, which is very close to the projectile energy gain or loss ΔE for a heavy target like C_{60}. By running many such trajectories, we build the angular- and energy-differential cross sections for specified target ionization stages. At present, we will concentrate on the most probable values of θ and the mean energy gain or loss values (ΔE_{mean}) as functions of the number of electrons r removed from C_{60} [cf. Eq. (1)]. These quantities are taken to be the maxima in $d\sigma/d\theta$ and the mean values of $d\sigma/d(\Delta E)$, respectively.

The sequence of critical distances R_r and the energy resonance condition yield projectile binding energies E_B^r according to

$$I_r+\frac{q-r+1}{R_r}=E_B^r+\frac{r}{R_r}-\frac{a(q-r+1)}{R_r^2-a^2}+\frac{a(q-r+1)}{R_r^2}$$
$$-\frac{a}{2R_r^2}+\frac{a}{2(R_r^2-a^2)}. \tag{13}$$

The left-hand side is the binding energy of the rth active electron when the projectile is at the distance R_r. The right-hand side is the resonant binding energy for the same electron localized to the projectile. The third and fourth terms to the right are the Stark shifts due to the image potential of the screened projectile charge $(q\text{-}r+1)$. The two last terms are due to the active electrons interaction with its own image charges when it is localized to the projectile. Note that Eq. (13) implies a quasicontinuum of projectile capture states since we assume that there always is a resonance with a projectile capture state

$$E_B^r=\frac{q-2r+1}{R_r}+\frac{a(q-r+1/2)}{R_r^2-a^2}-\frac{a(q-r+1/2)}{R_r^2}+I_r \tag{14}$$

when $R=R_r$. The lower bound for the total Q value for transfer of r electrons thus becomes

$$Q(r)=\sum_{i=1}^{i=r}(E_B^i-I_i). \tag{15}$$

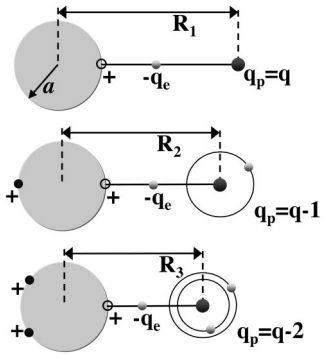

FIG. 5. Illustration of the model with movable and localized charges as the first, the second, and the third electron is transferred to the ion. The projectile charge seen by the first, second and third active electron is $q_p=q$, $q_p=q-1$, and $q_p=q-2$, respectively (cf. text).

Evaluation of Eq. (15) gives results in close agreement with those obtained by integration of the dynamically changing forces in the longitudinal direction. The effective quantum number for the first active electron is $n^1_{eff}=q\sqrt{1/2E^1_B}\approx 7.7$ according to Eq. (14). Taking the finite density of projectile capture states into account this indicates that the $n=7$ state should be dominant in pure single-electron capture, which is confirmed by experiments [7,21]. We finally note that Eq. (14) reduces to the corresponding expression for ion-atom collisions when $a\rightarrow 0$ [34].

B. Highly charged ions scattering on a sphere with movable point charges

In this second model we follow Shen *et al.* [15], Petrie *et al.* [16], and Cameron and Parks [17] and assume that the positive holes left behind on ionized C_{60} are movable on the molecular surface in a localized fashion. Schematics of the presently assumed mechanisms are indicated in Fig. 5.

When the projectile is at a distance $R\geqslant R_1$ from the center of the sphere, the binding energy of the first active electron to the positive hole on the surface of the sphere with radius $a=8.2a_0$ is

$$I^*_1=I_1+q/(R-a). \tag{16}$$

The positive hole is assumed to be localized closest to the projectile during the time it takes for the electron to move from the sphere to the ion. When the electron has reached the projectile, the positive hole moves towards the position that minimizes its potential energy. For a single hole ($r=1$) this position is obviously at the far side of the sphere. For distances R that are small enough to allow two electrons to be removed from the sphere ($r=2$) the equilibrium configuration forms a triangle with its corners at the two holes and the ion. Three holes on the surface ($r=3$) have a minimum of potential energy if they form an equilateral triangle with its surface normal pointing towards the ion. Thus the problems of finding the R-dependent forces on the holes and the ion become three dimensional when more than two electrons are active.

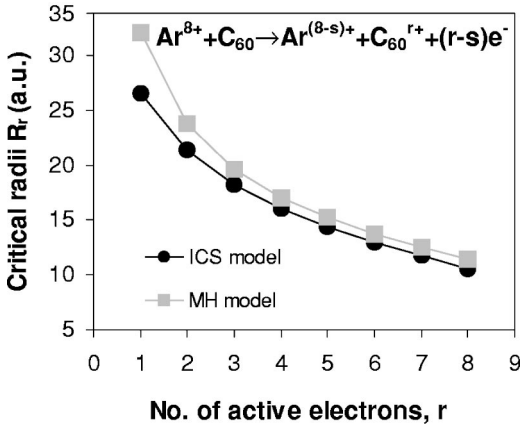

FIG. 6. The critical radii for electron transfer; R_r, according to the infinitely conducting-sphere (ICS, black circles) and the movable-hole (MH, gray squares) models. The lines between the data points are to guide the eye.

First, we perform a single-trajectory calculation with $b_{C_{60}}=0$ in order to determine the sequence of critical distances for electron transfer. We again assume full screening of the projectile charge. The energies required for ionization in the presence of the ion are given by $I^*_r=I_r+q_p/(R-a)$ with $q_p=q-r+1$. We follow the head-on trajectory ($b_{C_{60}}=0$) and solve the equations of motion for the holes and the projectile numerically. Oscillations in the hole positions are inherent in this model since the holes are always created in nonequilibrium positions (i.e., closest to the projectile). Therefore we have introduced a damping term for the hole motion, which has its physical basis in the scattering of moving charge carriers on electrons and nuclei (the electrical ''resistance''). The critical distances R_r are calculated by means of I^*_r and the electronic potentials between the target and the projectile. The latter are evaluated for the numerically determined positions of the $r-1$ holes, the projectile and the ''1+'' hole fixed on the surface closest to the projectile. The damping is chosen in order to allow the holes to find their equilibrium positions between sequential electron transfer events. For the present projectile velocity of $v\sim 0.2$ a.u. the times between the critical distances R_r lie in the range 0.1–1 fs, which implies hole-rearrangement times of the order of 10^{-16} s or faster. In view of orbital velocities (~ 1 a.u.) and the distances over which the charge carriers (holes) have to move ($\sim 10a_0$) this appears reasonable.

The first electron leaves the target at $R_1=32.1a_0$, the second at $R_2=23.8a_0$ and the eighth at $R_8=11.4a_0$. This R_r sequence is remarkably similar to the one for the infinitely conducting-sphere model as can be seen from the comparison in Fig. 6. The ICS model correctly accounts for polarization effects through the image charges, whereas no such effects are explicitly included in the movable-hole model. The positioning of the positive holes on the sphere surface are, however, able to give a fair representation of the electric field outside the sphere. This field becomes more similar to the electric field of the ICS model as r, the number of holes, increases (cf. Fig. 6).

The projectile angular scattering distributions are obtained

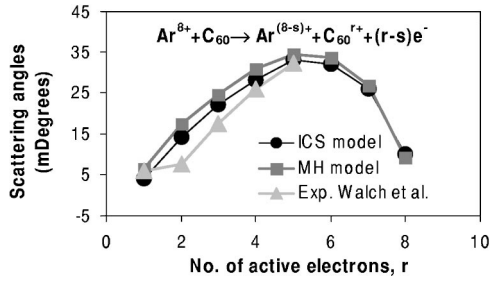

FIG. 7. The most likely scattering angles θ as functions of the number of active electrons (r) according to the infinitely conducting-sphere (ICS, black circles) and the movable-hole model (MH: gray squares). Energy-scaled experimental values by Walch *et al.* [23] measured in coincidence with intact (i.e., nonfragmenting) C_{60}^{r+} molecules are shown as gray triangles for $r=1-5$. The lines are to guide the eye.

by means of Monte Carlo calculations. For each trajectory, we solve the equations of motion for the projectile and the holes together taking the damping of the hole motion into account. As for the infinitely conducting-sphere model, $d\sigma/d\theta(r)$ are calculated by integrating the transversal momentum transfer to the projectile along many randomly selected trajectories. Again, the Q values are obtained by integrating the dynamically varying forces along the longitudinal direction.

The movable-hole model implies marginally larger θ than the infinitely conducting sphere model as can be seen in Fig. 7. In this figure, we have also included the energy-scaled results by Walch *et al.* [23] in which $d\sigma/d\theta$ were recorded in coincidence with *intact* C_{60}^{r+} molecular ions ($r=1-5$). These authors [23] also performed calculations based on a more elaborate version of the infinitely conducting-sphere model [8]. The results of Ref. [23] are in good agreement with both sets of present calculations after scaling with $E_0\theta=$ const from $E_0=2.5$ keV to $E_0=26.4$ keV.

In Fig. 8, we show the present two model predictions for $\Delta E_{mean}(r)$. The differences are minor and the agreement

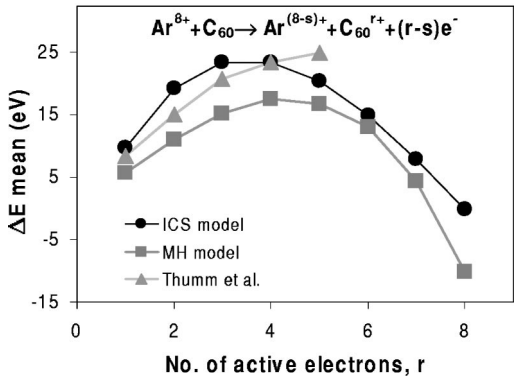

FIG. 8. Q values, obtained by integration of the forces along the ion trajectories in the infinitely conducting-sphere (ICS, black circles) and the movable hole (MH, gray squares) models. The model results by Thumm *et al.* [6] are shown as gray triangles. The lines are to guide the eye.

with Thumm *et al.* [6] is good in the region $r=1-5$. In contrast to Thumm *et al.* [6] and Walch *et al.* [23] we work with quantized charges, neglect recapture to the target, and allow the projectile to approach closer than the distance inside which fragmentation occurs [2]. The rational for the latter assumption is that the fragmentation time scale usually is much longer than the collision time. We thus find that it is possible to transfer eight electrons (sequentially) at distances well outside the radius of the model sphere when full screening of the projectile charge is assumed.

The electronic binding energies for the movable-hole model are related to the Q value through Eq. (15), which is a general expression used also for the infinitely conducting-sphere model. Both models predict capture into the $n=7$ shell in Ar^{8+}-$C_{60}\rightarrow Ar^{7+}$-$C_{60}^{+}$ collisions. As mentioned above, this has been established experimentally first by Selberg *et al.* [7] and later by Opitz *et al.* [21]. This conclusion is also supported by calculations by Thumm [8] and Bárány [14].

C. Monte Carlo calculations of close collisions

The infinitely conducting-sphere and movable-hole models both assume that the C_{60} molecule can be viewed as a completely smooth sphere. Therefore, we have also calculated the projectile scattering angles and energy gains or losses due to short-range interactions with the electron clouds and the nuclei of the 60 individual carbon atoms. Following Larsen *et al.* [35], we have used well-known formulas for electronic and nuclear stopping for this purpose.

The impact parameters with respect to the center of the C_{60} molecule, $b_{C_{60}}$ (cf. Fig. 4), are selected by means of a random-number generator. Three other random-number generators ensure that all orientations of the C_{60} molecule are equally likely just as in the real experiment. For each trajectory, atomic impact parameters b_k with k ranging from 1 to 60 are calculated for a randomly oriented C_{60} molecule. The total electronic energy transfer T_{el} is obtained as the sum of the individual energy transfers T_k^{el}, as given by the Firsov formula [35–37]. The total nuclear stopping power T_{Nuc} is the sum of 60 energy losses T_k^{Nuc} due to scattering on Ar-C Molière potentials with the screening lengths $a_s=0.25$ a.u. [38,39]. The Molière potential is also used to evaluate the sixty momentum-transfer vectors which give the total projectile scattering angle for close collisions.

In Fig. 9, we show Monte Carlo results for 16- and 26.4-keV Ar-C_{60} collisions.

The results for T_{Nuc} as functions of $b_{C_{60}}$ are given in the upper row. Each dot represents the result for an individual trajectory and, thus, the densities of dots are representative for the probabilities for the corresponding values of the energy loss. Note that a given value of $b_{C_{60}}$ may give rise to drastically different values of T_{Nuc}, due to different orientations of the C_{60} molecule. The curves in the upper row of Fig. 9 represent mean nuclear energy losses, which are rather constant for trajectories well inside the cage radius ($a_{cage}=6.7a_0$) and rise sharply when the atomic density increases as $b_{C_{60}}$ approaches a_{cage} (cf. Fig. 10).

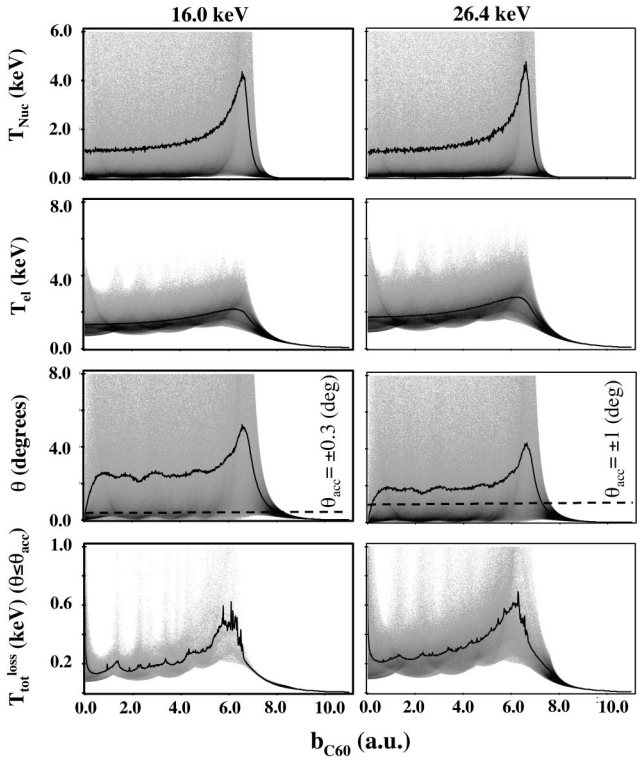

FIG. 9. Results from the Monte Carlo calculations for close collisions: Ar impact on 60 C atoms arranged in the geometry of a C_{60} molecule. Results for 16 and 26.4 keV are shown in the left and right columns, respectively. From the first to the fourth row we show as functions of $b_{C_{60}}$; nuclear energy loss T_{Nuc}, electronic energy loss T_{el}, projectile scattering angles θ, and the total energy loss T_{tot}^{loss} for a limited angular acceptance $\theta < \theta_{acc}$. In each case 3×10^6 trajectories have been launched and the densities of points are representative for the probabilities of the corresponding parameter values. The curves show the mean values.

The mean nuclear energy loss is *not* representative for the typical event since a few very hard collisions (very small b_k) contribute strongly to the mean value. Instead, the typical fate of a projectile passing through the C_{60} molecule is that it only loses a small amount of energy due to nuclear stopping.

The results for the electronic energy loss T_{el} are shown in the second row of Fig. 9. Also here the mean values (curves) are rather constant for trajectories well inside the molecule and increase when $b_{C_{60}}$ approaches a_{cage}. The edge effect is,

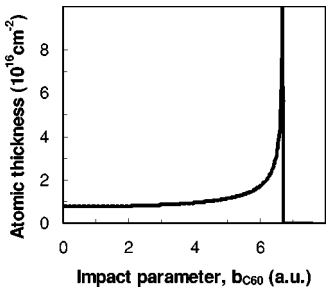

FIG. 10. The atomic thickness as a function of $b_{C_{60}}$ for a single C_{60} molecule.

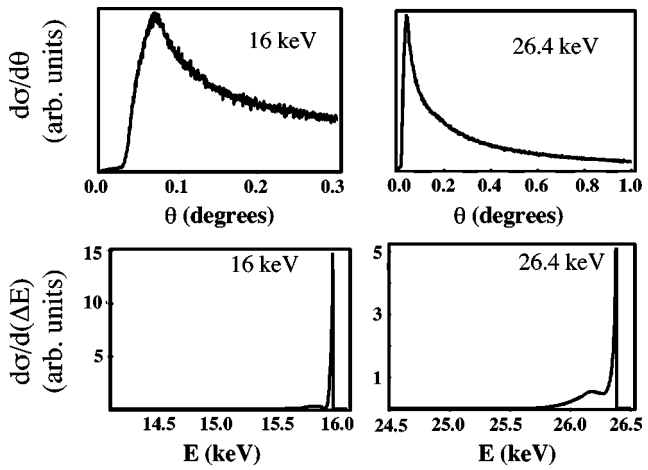

FIG. 11. The angular and energy differential cross sections $d\sigma/d\theta$ and $d\sigma/d(\Delta E)$ as functions of θ and the ion energy E after the collision. The results are calculated by means of randomly selected trajectories in the $b_{C_{60}}$ interval $(0–9.5)a_0$. The acceptance angles are $\pm0.3°$ and $\pm1°$ for 16 and 26.4 keV, respectively.

however, much less pronounced for T_{el} than for T_{Nuc}. The electronic energy loss, calculated by means of the Firsov formula [37], remains significant out to a few a_0 outside the molecule. The individual results for T_{el} fall closer to the mean value as $b_{C_{60}}$ increases for $b_{C_{60}} > a_{cage}$ since the orientation of the molecule then gradually becomes less important.

The third row of Fig. 9 shows the distributions of projectile scattering angles. Again the mean values are not really representative for the typical scattering that instead is indicated by the high density of points at low values of θ. The relevant experimental acceptance angles are shown and only trajectories below these lines should be used for comparisons with experiments. The fourth row displays the total energy loss T_{tot}^{loss}, which is the sum of T_{Nuc} and T_{el} for each trajectory inside the acceptance angle ($\theta < \theta_{acc}$). Clearly, the finite values of θ_{acc} discriminate against trajectories close to the periphery of C_{60}.

In Fig. 11, we show $d\sigma/d\theta$ calculated by means of the Monte Carlo results for $\theta(b_{C_{60}})$ (cf. Fig. 9).

There are strong increases in $d\sigma/d\theta$ at certain threshold values $\theta = \theta_{th}$ for both energies, which reflect the upper impact parameter chosen for the calculations [the range is $(0–9.5)a_0$]. The low intensities for $\theta < \theta_{th}$ are due to trajectories passing through C_{60}, a conclusion that we arrive at by performing calculations with $b_{C_{60}} < a_{cage}$ yielding wide $d\sigma/d\theta$ distributions that tend to zero as $\theta \to 0$. For $b_{C_{60}} > a_{cage}$, we only get contributions to $d\sigma/d\theta$ for $\theta > \theta_{th}$. The results for $d\sigma/d(\Delta E)$, based on $T_{tot}^{loss}(b_{C_{60}})$ for the impact parameter interval, $(0–9.5)a_0$, are also shown in Fig. 11. These spectra have two components; the humps at lower energies are due to collisions inside the C_{60} cage while the sharp peaks are due to outside trajectories. The dips between the humps and the peaks are due to scattering close to the periphery of the molecule giving angles larger than the acceptance. The relative intensities and the energy losses for the smaller peaks

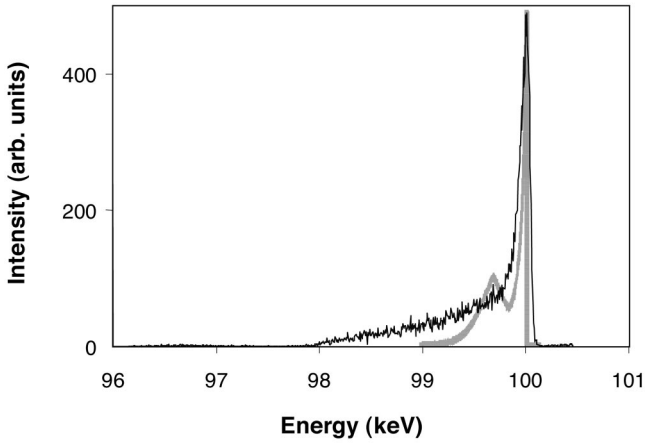

FIG. 12. Monte Carlo calculations of $d\sigma/dE$ for close Ar-C_{60} collisions [$b_{C_{60}}$: $(0-9.5)a_0$] at 100 keV (gray curve). The experimental results (black curve) for 100-keV Ar^{3+}-$C_{60}\rightarrow Ar^{+}$ are from Larsson *et al.* [40] with $\Delta\theta=\pm 0.5°$.

decrease with decreasing collision energy. We conclude that ion trajectories through the molecule are likely to give rise to large energy losses (dominated by electronic energy loss) and a rather wide range of scattering angles starting from $\theta=0$. Trajectories closely outside C_{60}, on the other hand, give rise to smaller energy losses but larger scattering angles ($\theta>\theta_{th}$).

In Fig. 12, we show a comparison between the presently calculated $d\sigma/d(\Delta E)$ and corresponding measurements for 100-keV Ar^{3+}-$C_{60}\rightarrow Ar^{+}$-$\cdots$ collisions by Larsson *et al.* [40].

The model results have not been convoluted with the experimental beam-energy spread.

The calculation is made with an angular acceptance of $\pm 0.5°$ (the same as in the experiment by Larsson *et al.* [40]) and an impact parameter interval $(0-9.5)a_0$. The comparison strongly indicates that the low-energy tail in the experimental distribution is due to trajectories through or closely outside the periphery of C_{60}. The calculation is, however, unable to reproduce the largest energy losses within the experimental angular acceptance. This is most likely due to a somewhat inadequate representation of the electron density and thus the electronic energy loss some distance outside a_{cage}.

IV. EXPERIMENTAL RESULTS AND DISCUSSIONS

A. Absolute charge-exchange cross sections and charge-state fractions

The present total charge-exchange cross section

$$\sigma_{tot}=\sum_{s=1}^{8}\sigma_s=6.6\times 10^{-14}\ \text{cm}^2 \tag{17}$$

is larger than the ones by Walch *et al.* at 80 keV [2] and Selberg *et al.* at 27 keV [7]. The latter, $\sigma_{tot}=(4.6\pm 1.4)\times 10^{-14}$ cm^2 [7] was obtained by means of the beam-attenuation method using setup *C* in Fig. 1 [7]. The infinitely

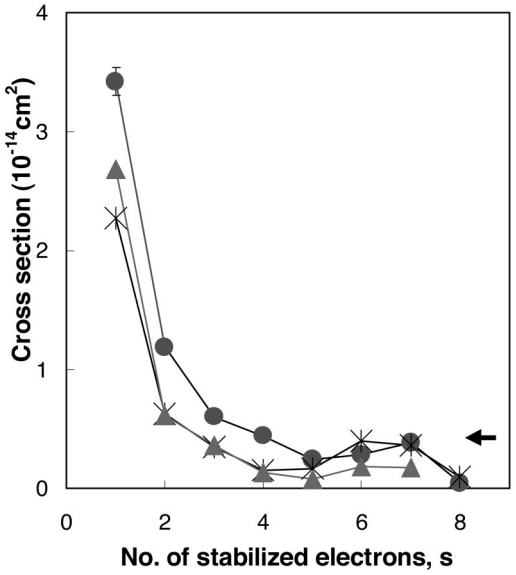

FIG. 13. Absolute cross sections for stabilizing one ($s=1$) through eight ($s=8$) electrons for Ar^{8+}-ion projectiles colliding with C_{60}. Present results at the collision energy 26.4 keV (filled circles), results of Walch *et al.* at 80 keV (crosses) [2] and by Martin *et al.* at 56 keV (filled triangles) [45]. All three sets of results rely directly or indirectly on the vapor pressure of Abrefah *et al.* [44] (cf. text). The geometrical cross section of the C_{60} cage (radius $a_{cage}=6.7a_0$) is indicated by the arrow. The lines between the data points are to guide the eye.

conducting-sphere and the movable-hole models predict $\sigma_{tot}^{ICS}=\pi R_1^2=6.2\times 10^{-14}$ cm^2 and $\sigma_{tot}^{MH}=\pi R_1^2=9.1\times 10^{-14}$ cm^2, respectively, and the present experimental results thus appear to favor the former prediction. However, the absolute cross-section scale has an uncertainty of roughly $\pm 50\%$ stemming from a spread in the literature values for the vapor pressure of C_{60} [41–44].

In Fig. 13 we show the present *s*-selective cross sections [cf. Eq. (1)] in comparisons with results by Walch *et al.* [2] and Martin *et al.* [45].

The present cross sections and the ones by Walch *et al.* [2] rely on the C_{60} pressure by Abrefah *et al.* [44], while the results by Martin *et al.* [45] at 56 keV have been normalized by means of $\sigma_{tot}=(4.4\pm 1.8)\times 10^{-14}$ cm^2 [2]. Our data were obtained with setup *B* (cf. Fig. 1), which allowed for detection of neutralized projectiles ($s=8$) with an acceptance angle of $\Delta\theta_B=\pm 1°$. Additional measurements with the smaller acceptance of setup *A* ($\Delta\theta_A=\pm 0.5°$) yielded consistent results for $s=1-7$.

The three sets of experimental results in Fig. 13 follow similar trends as functions of *s*. The hump around $s=6$ and $s=7$ appears in all three measurements, but is substantially weaker in the study by Martin *et al.* at 56 keV [45]. The origin of the hump is related to the *approach* of the charge-equilibration condition for projectiles passing through a single C_{60} molecule. This was pointed out already by Walch *et al.* [2] and the same conclusion was reached by Larsson *et al.* [40] in their interpretation of energy loss associated with two-electron capture in Ar^{3+}-C_{60} collisions. The equilibrium charge-state distribution is reached when the ioniza-

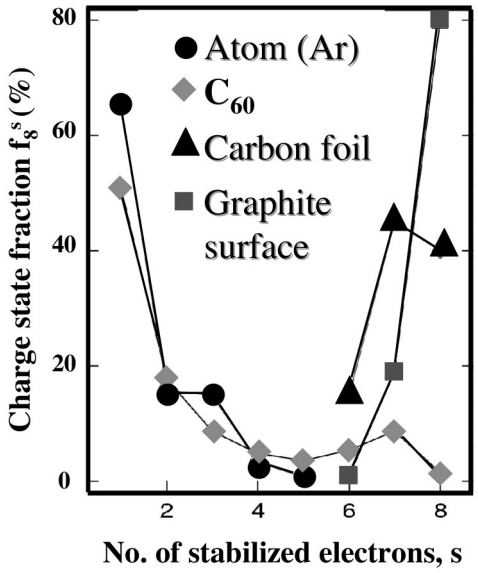

FIG. 14. Projectile charge state fractions $f_8^s = \sigma_s / (\Sigma_{s=1}^8 \sigma_s)$ as functions of the number of electrons, s, stabilized on incident Ar^{8+}-ion projectiles for different targets (cf. text).

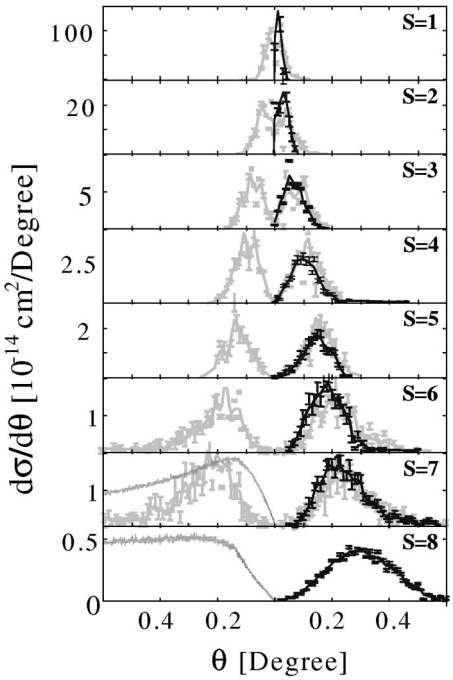

FIG. 15. Absolute experimental angular differential cross sections $d\sigma/d\theta$ for $s=1-8$. Two sets of results are shown; those obtained with the method B (for $s=1-8$; black data points) and those obtained with method A (for $s=1-7$; gray data points). Note the differences in cross-section scales for different s. The gray curves to the left in the $s=7$ and $s=8$ figures are Monte Carlo calculations for close collisions for the $b_{C_{60}}$ ranges (0–6) and (6–6.6)a_0, respectively.

tion and capture rates are equal, and its mean value defines the equilibrium charge. For Ar in carbon foils the latter quantity decreases from about 1 to about 0.5 when going from 100 to 26.4 keV [46]. For a fully charge-state equilibrated beam we would thus expect similar intensities for outgoing Ar^+ and Ar^0 at 26.4 keV, but this is clearly not the case (cf. Fig. 13).

There is no similar hump for large values of s in the s-selective cross sections for O^{8+}-C_{60} collisions [5]. This is most likely due to the fact that O^{8+}, in contrast to Ar^{8+}, carries K- and L-shell vacancies into the collision. Thus, electrons in the M shell of oxygen (but not argon) may be efficiently emitted in downstream Auger relaxation processes.

In Fig. 14 we show the final charge-state distributions for Ar^{8+} ions interacting with Ar, C_{60}, a graphite surface, and a carbon foil.

The charge-state distribution for the Ar-ion target is obtained at 80 keV by Ali *et al.* [47] and the C_{60} results are from the present data at 26.4 keV. Winecki *et al.* [48] measured the outgoing charge-state distribution for 51-keV Ar^{8+}-ions incident at 1.6° on a graphite surface. Finally, the charge-equilibrium distribution for 100-keV Ar through a carbon foil was obtained from Turkenburg *et al.* [49]. For the C_{60} and the Ar-targets the charge-state distributions decrease in a similar way up to $s=4$, while the charge-state fraction for C_{60} is significantly larger than for the atomic target when $s=5$. The C_{60} result resembles the one for the carbon foil for $s \geq 6$, which indicates that the hump for C_{60} is related to projectile trajectories through, or close to, the nuclear structure of the molecule. We note again, however, that the neutral component for the C_{60} collisions is lower than for the charge-state equilibrium case and, thus, that this condition is not fully reached for passage of a single C_{60} molecule.

B. Angular differential cross sections $d\sigma/d\theta$

The absolute angular differential cross sections $d\sigma/d\theta$ for processes (1) with s ranging from one to eight are shown in Fig. 15.

The two sets of measurements are performed with the cylindrical analyzer (system A in Fig. 1) and with the small-angle deflector (system B). The agreement is satisfying considering the very different images on the detector for A and B (cf. Fig. 1). The results for setup A are double sided, i.e., $d\sigma/d\theta$ is measured both up and down in the vertical direction (the analyzer is focusing in the horizontal direction). The spectra obtained with B are only single sided due to the asymmetry of the image on the two-dimensional detector (cf. Fig. 1). We deliberately chose this asymmetric picture, caused by a slight misalignment of the gas cell, in order to increase the angular acceptance in one direction. The agreement between the two sets of results also shows that even the smaller acceptance angle of setup A was sufficient ($\Delta\theta_A = \pm 0.5°$ and $\Delta\theta_B = \pm 1°$).

On the average, the projectile scattering angles become larger as s increases. The shapes of $d\sigma(s)/d\theta$ are symmetric up to $s=5$, but for $s=6$, and in particular $s=7$, they become asymmetric with tails to the high-θ sides. Typical scattering angles are significantly larger for the neutralizing collisions ($s=8$) and the spread in scattering angles becomes larger, i.e., $d\sigma/d\theta$ becomes wider. From the comparison of projectile charge-state distributions presented in Fig. 14 we have

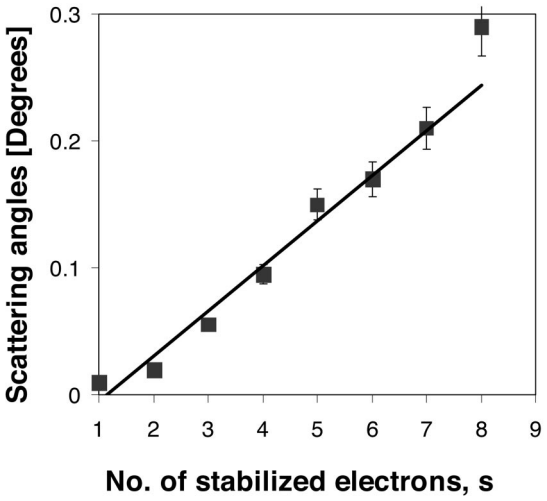

FIG. 16. The most probable deflection angles θ as function of the number of electrons s, stabilized on the incident Ar^{8+}-ion projectile. The line is a fit to the data for $s \leqslant 7$.

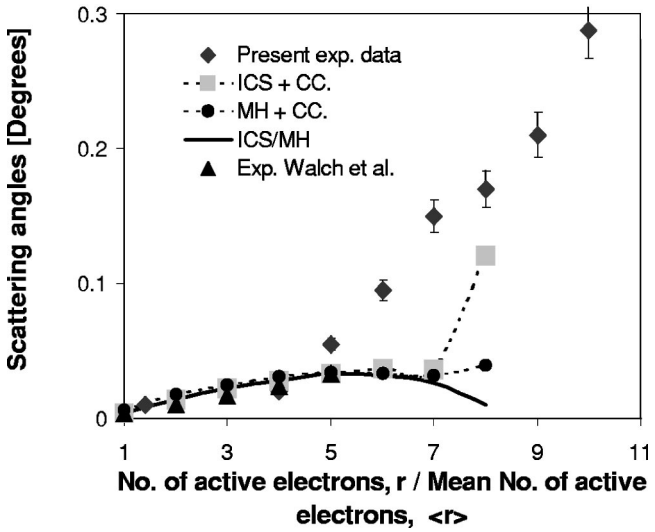

FIG. 17. The present most likely experimental scattering angles θ as functions of the mean numbers of active electrons $\langle r \rangle$ in 26.4-keV Ar^{8+}-C_{60} collisions. We have used the relation $\langle r \rangle = s + 2$ by Martin *et al.* [45] for $r \geqslant 2$. For $s = 1$, we use $\langle r \rangle = 1.4$ from Sec. IV D and [45]. The results from the infinitely conducting-sphere (ICS) and movable-hole (MH) models, as functions of r, are shown alone (full black curve) and with the inclusions of the contributions from close collisions (''ICS+CC'' and ''MH+CC''). The results from [23] (Walch *et al.*; triangles), scaled from $E_0 = 2.5$ keV to $E_0 = 26.4$ keV, are shown as functions of r.

already concluded that the intensities for $s = 7$ and 8 at least in part are due to trajectories through C_{60}. Since the atomic density is larger close to the periphery of the molecule, it appears reasonable to assume that the $s = 8$ intensity mostly is dominated by impact parameters around the periphery while the $s = 7$ intensity partly is due to smaller $b_{C_{60}}$. Indeed our Monte Carlo calculations for close collisions give $d\sigma/d\theta$ resembling the experimental ones for the impact parameter ranges $b_{C_{60}} = 0 \rightarrow 6$ a.u. ($s = 7$) and $b_{C_{60}} = 6 \rightarrow 6.6$ a.u. ($s = 8$) as can be seen in Fig. 15.

In Fig. 16, we show the results for the most probable scattering angles, obtained as the positions of the maxima of $d\sigma/d\theta$ in Fig. 15.

These positions increase linearly with s up to $s = 7$. For $s = 8$, the value lies above the line fitted for $s \leqslant 7$. This monotonic behavior appears somewhat surprising in view of the very different processes that are active in distant (soft) and close (hard) collisions. In the distant collisions, well outside the C_{60} cage, relatively few electrons are removed softly from the target and the projectile scattering is well described by the infinitely conducting-sphere and the movable-hole models. This has already been shown in the comparison of Fig. 7. The energy transferred to the molecule in soft collisions (large $b_{C_{60}}$) is minor according to the close-collision Monte Carlo calculations of Sec. III C (cf. Fig. 9). In the closer collisions, scattering on individual carbon nuclei becomes important and fairly large amounts of energy are transferred to the target. The importance of the close collisions for large s becomes directly evident by comparing the s and r dependencies of θ in Figs. 16 and 7, respectively. In the latter, θ reached a maximum at $r = 5$ while θ increases monotonically with s in Fig. 16.

In Fig. 17, we again show the present most likely projectile-scattering angles, but now as functions of the average number of electrons $\langle r \rangle$ removed from C_{60}.

Martin *et al.* [45] established the relation $\langle r \rangle = s + 2$ ($s \geqslant 2$) for Ar^{8+}-C_{60} by measuring s in coincidence with the total number of emitted electrons ($r - s$). Note that $\langle r \rangle = s + 2$ only is valid for the present collision system and that the relation between r and s may be very different for other systems (cf. O^{8+}-C_{60} [5]). The present measurements indicate slightly higher θ for $r = 5$ than the energy-scaled results from Ref. [23]. This is most likely due to the fact that our noncoincidence measurements automatically include the somewhat harder scattering events leading to fragmentation. The predictions of the infinitely conducting-sphere and movable-hole models alone are clearly inadequate for describing processes with many active electrons since the C_{60} molecule is not a smooth sphere but has an internal structure.

Therefore, we define total scattering angles for a given value of r by simply adding the relevant average close-collision contributions, θ_{CC}^{ICS} or θ_{CC}^{MH}, for the appropriate impact parameter ranges $R_{r+1}^{ICS} \leqslant b_{C_{60}} \leqslant R_r^{ICS}$ and $R_{r+1}^{MH} \leqslant b_{C_{60}} \leqslant R_r^{MH}$. The total most likely scattering angle $\theta_{tot}^{ICS}(r)$ obtained from the infinitely conducting-sphere model in combination with close collisions for r active electrons thus becomes

$$\theta_{tot}^{ICS}(r) = \theta^{ICS}(r) + \theta_{CC}^{ICS}(r). \tag{18}$$

Similarly we get

$$\theta_{tot}^{MH}(r) = \theta^{MH}(r) + \theta_{CC}^{MH}(r) \tag{19}$$

when combining the movable-hole model with the close-collision results. For a given r, $R_r^{MH} > R_r^{ICS}$, and $\theta_{CC}^{MH} < \theta_{CC}^{ICS}$. This procedure gives marginally larger predictions

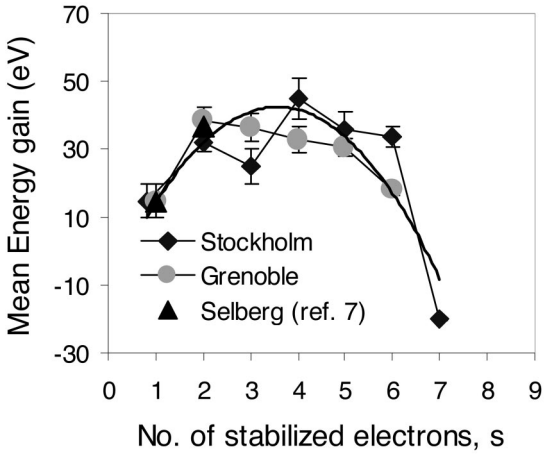

FIG. 18. The mean experimental energy gain or loss, ΔE_{mean}, as a function of s for $Ar^{8+}+C_{60}$ collisions. The data are from Stockholm (26.4 keV; black diamonds) and Grenoble (16 keV; gray circles). The additional high-precision results shown for $s=1$ and $s=2$ are the mean values of the high resolution ΔE spectra by Selberg *et al.* [7]. The lines between the data points are to guide the eye. The thick black curve is a fit to the data.

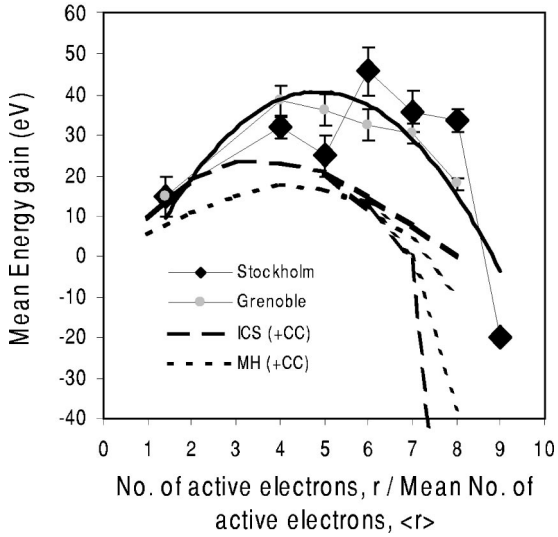

FIG. 19. The mean energy gain or loss, ΔE_{mean}, as a function of the mean number of active electrons, $\langle r\rangle$, for $Ar^{8+}+C_{60}$ collisions. The relation $\langle r\rangle = s+2$ by Martin *et al.* [45] is used to connect the present experimental data from Stockholm (26.4 keV; black diamonds) and Grenoble (16 keV; gray circles) to the $\langle r\rangle$ scale. The lines between the data points are to guide the eye. The long-dashed lines show the infinitely conducting sphere results alone (ICS; upper branch) and with the close collisions added (ICS +CC; lower branch). The short-dashed lines show the movable-hole model results alone (MH; upper branch) and with the close collisions added (MH+CC; lower branch).

for the total scattering angles except for $r=8$ as can be seen in Fig. 17. For $r=8$, the close collisions give the dominant contributions to the scattering angles for both the ICS and MH models. Neither the ICS nor the MH model allow for removal of more than eight electrons from C_{60} and therefore we have assumed that the impact parameter ranges $0 \leqslant b_{C_{60}} \leqslant R_8^{ICS}$ and $0 \leqslant b_{C_{60}} \leqslant R_8^{MH}$ contribute to $\theta_{CC}^{ICS}(r=8)$ and $\theta_{CC}^{MH}(r=8)$, respectively. The ICS result for $r=8$ is close to the experimental value for $\langle r\rangle = 8$, while the inclusion of close collisions is unable to fill the gap between the models and the experiment for $\langle r\rangle = 7$ and $\langle r\rangle = 6$. This discrepancy is partly explained by the fact that we compare model results for well specified values of r with experimental results for average values of r. The measured angular distributions of course contain contributions for $r > \langle r\rangle$.

C. Translational energy gain and loss

The mean translational energy gain or loss as a function of s is shown in Fig. 18 for the present 16- and 26.4-keV Ar^{8+}-C_{60} collisions.

The corresponding data for $s=1$ and $s=2$, deduced from the high-resolution energy gain spectra by Selberg *et al.* [7] are also shown. The Stockholm (26.4 keV) and the Grenoble (16 keV) data agree within error bars between $s=1$ and $s=5$. For $s=1$ and 2 both sets are in agreement with the result of Selberg *et al.* [7]. The much smaller error bars for the latter measurements are due to the special technique in which the ion beam was retarded strongly after the collision cell but before the energy analysis [7]. The main purpose of the present study, however, is to determine whether or not multiple-electron transfer processes mostly are associated with projectile energy gain ($\Delta E_{mean} > 0$) or loss ($\Delta E_{mean} < 0$). The measured values of ΔE_{mean} first increase from 15 ± 6 eV to 32 ± 5 eV between $s=1$ and $s=2$ and then they change little up to $s=6$. Finally there is a rather strong decrease yielding a dominance of energy loss $\Delta E_{mean} = -20 \pm 5$ eV for $s=7$.

The translational energy gain or loss, i.e., the change in the kinetic energy of the projectile, reflects the rearrangement between potential and kinetic energy in the collision. Positive contributions to ΔE_{mean} are obtained when electrons are captured from the target to projectile states with larger binding energies. This is, for instance, the case when the first active electron is removed from the target with binding energy I_1 and is captured into the more tightly bound $n=7$ state of Ar^{7+} ion. It has been shown by Selberg *et al.* [7] and Opitz *et al.* [21] that the internal excitation (heating) of the C_{60} molecule indeed can be neglected for such distant collisions. For closer collisions, however, the energy transfer to the molecule has to be taken into account. In Fig. 19 we also show theoretical Q values calculated by means of the infinitely conducting-sphere and the movable-hole models in comparisons with the experimental results.

The internal excitations of the target due to close collisions (cf. Sec. III C) are included according to

$$Q_{tot}^{ICS}(r) = Q^{ICS}(r) - T_{tot}^{loss}(R_{r+1}^{ICS} \leqslant b_{C_{60}} \leqslant R_r^{ICS}) \quad (20)$$

and

$$Q_{tot}^{MH}(r) = Q^{MH}(r) - T_{tot}^{loss}(R_{r+1}^{MH} \leqslant b_{C_{60}} \leqslant R_r^{MH}), \quad (21)$$

where the values of T_{tot}^{loss} are obtained by means of the close-collision calculations of Sec. III C. The infinitely conducting-

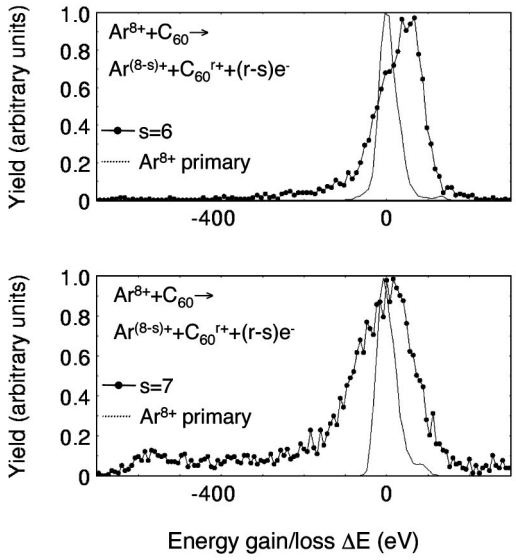

FIG. 20. The measured energy gain or loss distributions for Ar ions emerging in charge states $2+$ ($s=6$; above) and $1+$ ($s=7$; below). The energy profiles of the corresponding primary Ar^{8+}-beams are shown for comparisons. The lines between the data points are to guide the eye.

sphere model predicts slightly larger values of ΔE_{mean} than the movable-hole model for all values of $\langle r \rangle$. Both sets of model predictions are lower bounds to the Q values since we have assumed quasicontinua of projectile capture states (cf. Secs. III A and III B). Consequently the model results lie below the experimental values, which are shifted according to $\langle r \rangle = s+2$ for $s \geq 2$ [45]. The models correctly account for the flat maximum in ΔE_{mean} as a function of $\langle r \rangle$ and the falloff to negative values of ΔE_{mean} at larger $\langle r \rangle$. The latter effect occur in the smooth-sphere models alone but is emphasized by the internal target excitations due to the close collisions. Note that the ICS+CC model predicts larger excitations of C_{60} than MH+CC for a given r due to the somewhat smaller values of R_r (cf. Fig. 6).

The ΔE distributions for $s=6$ and $s=7$ are shown in comparison with the energy widths of the corresponding primary Ar^{8+} beams in Fig. 20.

According to the calculations of Sec. III C, projectiles with impact parameters $b_{C_{60}} < R_7$ lead to substantial internal heating of the molecule. For even smaller $b_{C_{60}}, T_{tot}^{loss}$ increases strongly approaching a few hundred eV as $b_{C_{60}}$ gets closer to and smaller than a_{cage}. This is qualitatively in agreement with the experimental observations of a rather strong energy loss component for $s=7$ (cf. Fig. 20), the hump in the charge-state distribution (cf. Figs. 13 and 14) and the wide angular scattering distribution (cf. Fig. 15) for $s=7$.

D. Fragmentation

The total spectrum of recoiling intact and fragmenting C_{60}^{r+} ions, i.e., integrated over ΔE and s were measured at CEA Grenoble with the technique described in Sec. II B.

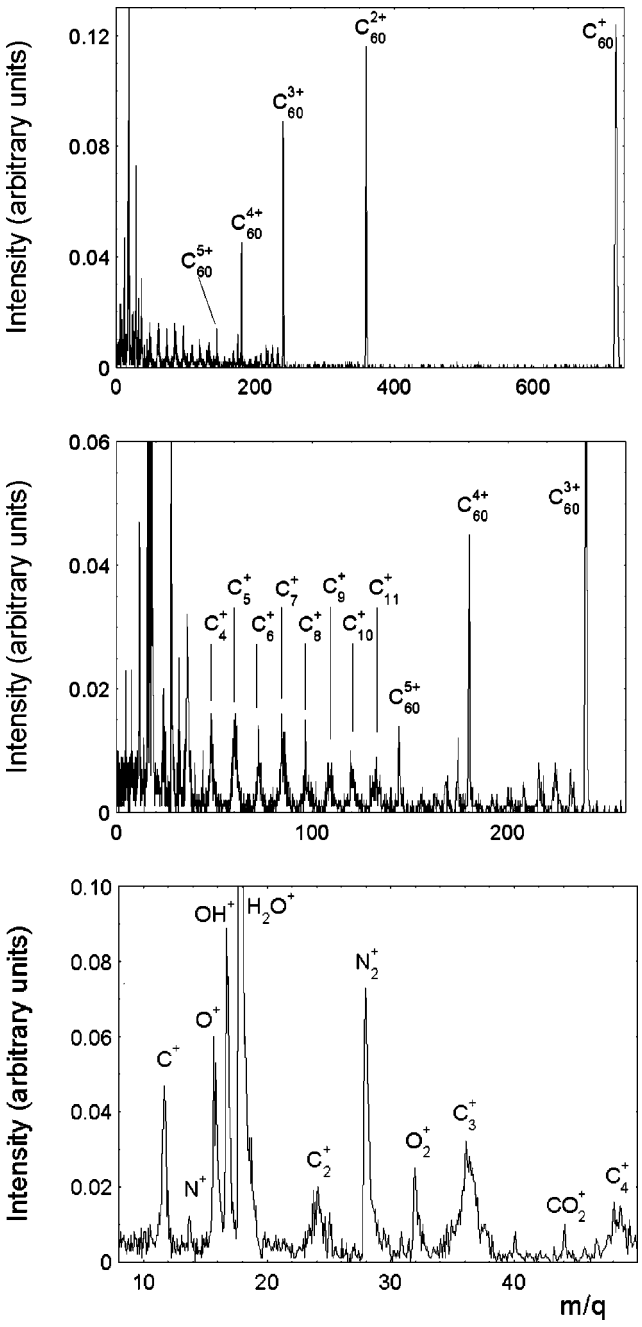

FIG. 21. The total distribution of recoiling intact and fragmenting C_{60}^{r+} ions due to 16-keV Ar^{8+}-C_{60} collisions integrated over s and ΔE. These data are obtained by using a pulsed Ar^{8+} beam and a pulsed extraction voltage. The projectiles are not detected. The mass-to-charge (m/q) distribution in the range 0–730 amu is shown on top, while different details of the same distribution are shown in the middle (0–250 amu) and the bottom (0–50 amu) figures. The data acquisition system has multihit capability, i.e., several fragments from the same collision event may be detected.

Prominent narrow peaks corresponding to intact C_{60}^{+} through C_{60}^{5+} are clearly visible in Fig. 21.

No heavy fragments appear between C_{60}^{+} and C_{60}^{2+}, which shows that C_{60}^{+} always is produced by cold electron capture to the projectile at large impact parameters. Between

C_{60}^{2+} and C_{60}^{3+}, there are some very weak peaks in the region around C_{50}^{2+} but there is no trace of a C_{60-2m}^{2+} series characteristic of sequential C_2 emission from internally excited C_{60}^{2+} [50]. Thus, in the cases where C_{60}^{2+} recoils are produced, there is an overwhelming probability that they stay intact. Between C_{60}^{3+} and C_{60}^{4+}, clearly visible but rather weak peaks due to C_{60-2m}^{3+} with m ranging from one to six appear (cf. Fig. 21). Again, however, the intensity distribution on these fragments is not the one for sequential emission of C_2 fragments. Instead, coincidence measurements show that the C_{60-2m}^{3+} peaks mostly appear together with C_2^+ or C_4^+ fragments (cf. Opitz *et al.* [21]) and thus that they stem from fragmentation of C_{60}^{r+} with $r \geqslant 4$. We conclude that also C_{60}^{3+} for the most part are created sufficiently cold to stay intact.

For C_{60}^{4+}, the situation is different in that the summed cross section for production of C_{60-2m}^{4+} is about equal to the cross section for production of intact C_{60}^{4+}. Further, the intensities of the fragment peaks decrease with m in the way expected for sequential C_2 emission [18]. Fragmentation is dominant for C_{60}^{6+} and higher charges as is evidenced by the absence of narrow peaks at, e.g., $m/q=120$. There is a broader peak at $m/q=120$ but it is mainly due to C_{10}^+ fragments, which have wider distributions in the kinetic energy releases due to the fragmentation process.

The light fragment peaks, C_1^+ through C_{11}^+, in Fig. 21 are all kinematically broadened, even though we note that C_1^+ is narrower than the other peaks in this group.

The intensity as a function of the number of C atoms in the C_1^+-C_{11}^+ range strongly resembles the one reported by Nakai *et al.* [51] for fast 15.6-MeV C^{6+}-C_{60} collisions. Similar patterns have also been observed after slow He^+-C_{60} [20] and O^{6+}-C_{60} collisions [52] and in photoionization experiments [53]. This seems to suggest that the C_1^+-C_{11}^+ sequence reflects fundamental breakup features of C_{60} rather than the exact nature of the ionizing process.

In Fig. 22, we display the fragmentation patterns recorded in coincidence with various outgoing projectile charge states, Ar^{8+}-$C_{60} \rightarrow Ar^{(8-s)+}$-$\cdots$, for the cases $s=1$–4, and $s=6$. For $s=1$, only intact C_{60} recoiling molecular ions of charge states up to four are seen. Already for outgoing Ar^{6+} ($s=2$), substantial fragmentation occurs. Intact molecules with charge states up to at least 6+ are observed and the fragments are dominated by heavy ones stemming from the breakup of C_{60}^{r+} with $r \geqslant 4$. Light charged fragments like C_2^+ and C_4^+ that are observed in coincidence with Ar^{6+} ($s=2$) appear as correlated with heavy fragments of charges three or higher (Opitz *et al.* [22]). In all, about 50% of the intensity in the $s=2$ spectrum is due to fragmentation. The intact molecules C_{60}^{4+}, C_{60}^{5+}, and C_{60}^{6+} are comparatively few (less than 5% of the total spectrum) when measured in coincidence with outgoing Ar^{5+} ions ($s=3$). Instead light, singly charged fragments dominate with a maximum for C_7^+ at $s=3$. There are no detected intact molecules for $s=4$ and now C_3^+ and C_1^+ grow in magnitude compared to the $s=3$ channel. For outgoing Ar^{2+} ions ($s=6$) only C_1^+ through C_4^+ fragments appear with the lighter ones being the most common. By means of the

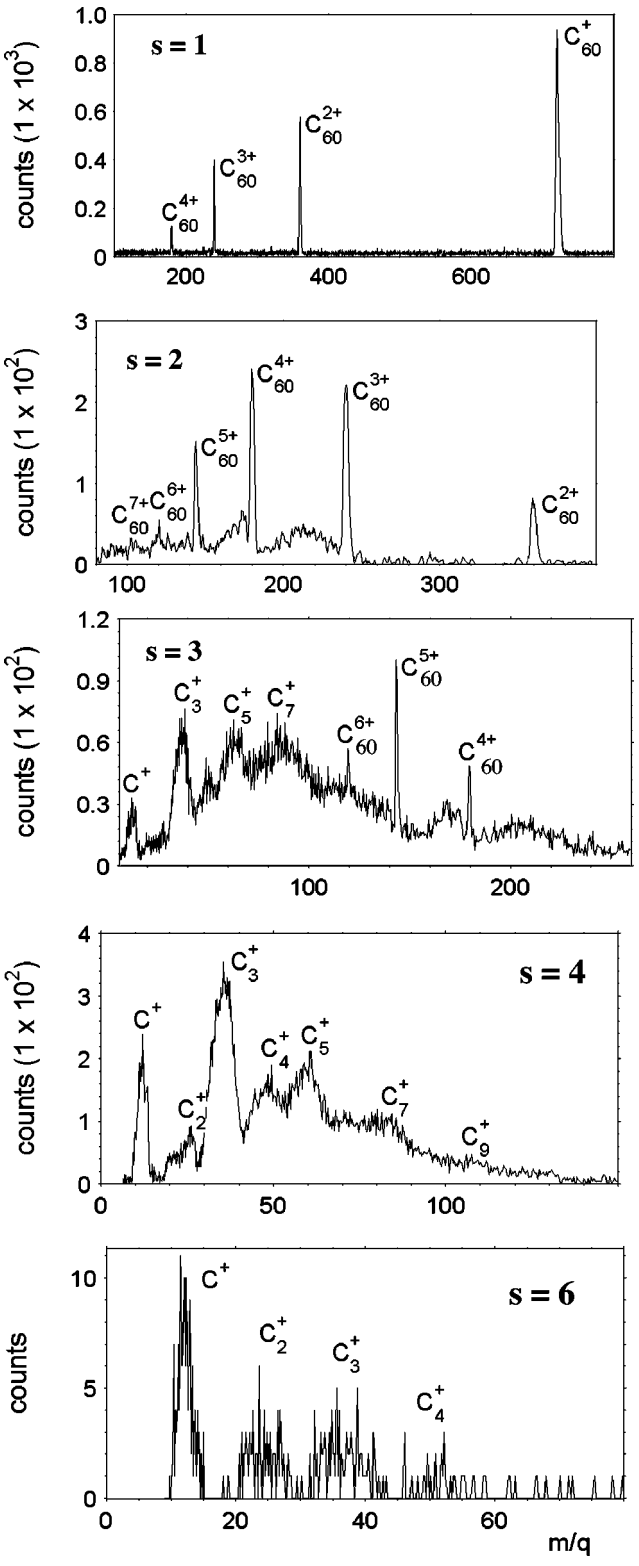

FIG. 22. The fragmentation spectra measured in coincidence with different outgoing projectile charge states $q'=(8-s)$ with $s=1$–4 and $s=6$ for 16 keV Ar^{8+}-C_{60} collisions. These spectra are obtained by integrations over the respective energy gain or loss distributions and an acceptance angle of $\pm 0.3°$.

absolute-charge exchange cross sections as a function of s (cf. Fig. 13) and the fractions in the various spectra of Fig.

21 that contribute to fragmentation, we arrive at a total experimental cross section of $\sigma_{tot}^{fragm}=2.6\times10^{-14}$ cm^2. This indicates a geometrical critical radius for fragmentation of $R_{fragm}=17a_0$.

The critical radii for C_{60}^{4+} production are $R_4^{ICS}=16$ and $R_4^{MH}=17a_0$ according to the infinitely conducting-sphere and movable-hole models, respectively. From this point of view an onset of fragmentation for C_{60}^{4+} at distances around $17a_0$ appear reasonable. However, our Monte Carlo calculations for close collisions gives total energy transfers to C_{60} well below 1 eV for such comparatively large distances. A possible explanation to why we still observe evaporative fragmentation as far out as $17a_0$ could in principle be that C_{60}^{4+} also is produced in much closer collisions. If this would be the case we would also expect some fragmentation of C_{60}^{3+} due to its production at distances considerably smaller than R_3. Since this is not observed it appears basically correct to assume that C_{60}^{r+} are produced within rather well-defined radial intervals $R_{r+1}<R<R_r$ (at least for distances well outside a_{cage}). Instead, a more likely explanation is that T_{tot}^{loss}, i.e., the internal excitation of the target, is underestimated in our Monte Carlo calculations for close collisions (cf. Sec. III C). Obviously, our model target of 60 *unperturbed* carbon atoms positioned in the corners of a truncated icosahedron gives much to low values of the energy loss a few a_0 outside $a_{cage}=6.7a_0$ (cf. Sec. III C).

Campbell, Raz, and Levine [19] have suggested a statistical model to account for the different fragmentation modes of C_{60} as a function of the internal temperature. According to Ref. [19], there is a phase transition in neutral and singly charged C_{60} around $T=4000$ K. That is, the temperature is almost constant for internal excitation energies in the range 80–225 eV. The statistical model, which has been successfully applied to e.g., slow C_{60}^{+}-Ar collisions [19,54], predicts emission (sequential) of light fragments below 80 eV, the bimodal fragmentation pattern in the intermediate region, and catastrophic destruction into small fragments above 225 eV. This statistical approach implies very fast coupling between the vibrational and electronic degrees of freedom such that only the *total* internal excitation energy (vibrational plus electronic) influences the fragmentation process. This view is supported by the strong similarities of the C_1^{+}-C_{11}^{+} fragment distributions for different excitation methods [20,51–53] and is further underscored by the present C_1^{+}-C_{11}^{+} results (Fig. 21).

The opposite view is taken by Schlathölter *et al.* [20] who have investigated the velocity dependences of the fragmentation patterns following He^{+}-C_{60} collisions. Their results strongly indicate that it is possible to separate evaporative fragmentation due to vibrational excitation through nuclear scattering and catastrophic fragmentation due to molecular heating through electronic energy loss [20]. That is, the fragmentation takes place before the excitation energy has had time to distribute between the vibrational and electronic degrees of freedom. Schlathölter *et al.* also observed a gradual and smooth transition from evaporative to catastrophic fragmentation as the collision velocity was increased and thus concluded that there is no phase transition in the C_{60} molecule [20].

The present fragmentation results do not allow us to reach a definite conclusion regarding the relations between the excitation and fragmentation processes. Our total fragmentation spectrum (cf. Fig. 21) shows a gradual change from nonfragmenting cold capture for C_{60}^{r+} ($r=1-3$) to evaporative fragmentation and fission for C_{60}^{r+} ($r=4$ and 5). For higher r catastrophic fragmentation occurs. Qualitatively this behaviur is expected from the statistical model [19] but it does occur at much larger distances than predicted by our Monte Carlo calculations. The contents of Fig. 22, showing the fragmentation for $s=1-4$ and $s=6$ could be used to define average internal excitation energies, since there is a clear relation between the most likely projectile scattering angle and the number of electrons s, stabilized on the projectile (cf. Fig. 16). The $s=1$ spectrum is completely dominated by cold capture and spectra associated with stabilization of three or more electrons are strongly dominated by catastrophic fragmentation. For $s=2$ there is a mixture of cold capture, evaporative fragmentation and fission, which according to the statistical model should be associated with excitation energies in the 50–200 eV range (the region for the predicted phase transition [19]). Again, however, these energies are much higher than predicted by our close-collision calculations.

V. CONCLUSIONS

The main theme of the present work has been to use measurements of projectile angular differential cross sections and energy gain or loss in order to probe the electronic response of single C_{60} molecules. In the infinitely conducting sphere model we assumed that the motion of active electrons on the target was fast enough to wash out all effects of charge localization during the collision. In contrast, the electronic response time could be varied in the movable-hole model such that effects of the localization of individual charge carriers (positive holes) could be seen. For more than a few active electrons the two model results are very close if we allow the holes in the MH model to reach new equilibrium positions between sequential over-the-barrier electron transfers. The excellent agreement between the two models and the experimental results for 26.4-keV Ar^{8+}-C_{60} collisions indicates an electronic response time of 10^{-16} s or shorter. We thus conclude that the electrons in the HOMO band of ionized C_{60} are highly mobile and that the ''electric conductivities'' of these molecular ions are high.

Another important goal has been to discriminate between the ICS and the MH models. This is difficult since they give similar results for the angular scattering and the energy gain. There are, however, some differences and general arguments that appear to be more supportive of the ICS model. An obvious shortcoming of the MH model is that projectile trajectories will remain undeflected until the first electron is transferred. The reason for this is that only the positive ''holes'' moving on the surface of the sphere contribute to the external electric field and therefore there is no attraction between the projectile and neutral C_{60} before electron trans-

fer. The first critical distance for over-the-barrier transfer is significantly larger in the MH than in the ICS model for basically the same reason. The latter model thus appears to be favored by the present measurements (assuming that the vapor pressure of Abrefah *et al.* [44] is correct). These arguments should not, however, be taken as an indication that the movable-hole model is of no use. On the contrary, the possibility to control the electronic response time in this model could be used to investigate electronic mobilities in other large molecules as, e.g., biomolecules. Further, there are still a number of experimental observations that so far only have been explained within the MH model as, e.g., the large nonfragmenting electron capture cross-sections in fullerene-fullerene collisions [15].

The ICS and MH model spheres are completely smooth and thus they cannot be used to describe the scattering in closer collisions where interactions with individual carbon atoms are important. For 26.4-keV Ar^{8+}-C_{60} collisions with eight active electrons we measured typical scattering angles in excess of 150 mdeg, while the ICS and the MH models predict $\theta < 10$ mdeg. Monte Carlo calculations for scattering on 60 Ar-C Molière potentials arranged in the geometry of a truncated icosahedron have been used to account for this observation. There are, however, several other close-collision phenomena that remain to be explained such as, e.g., the large critical radius for fragmentation ($17a_0$). This indicates that the energy transfer to the molecule, dominated by electronic energy loss, is underestimated at distances some atomic units outside the molecular cage. The model C_{60} target with 60 unperturbed carbon atoms probably leads to an underestimation of the radial extension of the molecular electron cloud.

There are many very intriguing phenomena in the field of slow ion-C_{60} collisions that still are unexplained; the observation of very high secondary electron emission yields in collisions with highly charged ions; the statistical or nonstatistical nature of the fragmentation process; the possible existence of a phase transition in C_{60}, and the stability limit for highly charged C_{60}^{q+}. These issues have merely been touched upon in the present work where the main discussion has been centered on the electronic response of C_{60} and the gross phenomena associated with contributions from close collisions.

ACKNOWLEDGMENTS

The experiments have been performed at the Manne Siegbahn Laboraty in Stockholm and at the AIM accelerator, a facility of CEA Grenoble. Fruitful discussions with Anders Bárány and Lotten Hägg at Stockholm University and Uwe Thumm from Kansas State University are gratefully acknowledged. This work was supported by the Swedish Research Council under Contract No. F-AA/FU 08801-325.

[1] M. S. Dresselhaus, G. Dresselhaus, and P. C. Eklund, *Science of Fullerenes and Carbon Nanotubes* (Academic Press, San Diego, 1995).
[2] B. Walch, C. L. Cocke, R. Voelpel, and E. Salzborn, Phys. Rev. Lett. **72**, 1439 (1994).
[3] J. Jin, H. Khemliche, M. H. Prior, and Z. Xie, Phys. Rev. A **53**, 615 (1996).
[4] A. Brenac, F. Chandezon, H. Lebius, A. Pesnelle, S. Tomita, and B. A. Huber, in *Proceedings of the IX International Conference on the Physics of Highly Charged Ions, Bensheim, Germany, 1998*, edited by P. H. Mokler, F. Bosch, Th. Stöhlker, and A. Wolf [Phys. Scr. **T80**, 195 (1999)].
[5] L. Chen *et al.*, in *Proceedings of the IX International Conference on the Physics of Highly Charged Ions, Bensheim, Germany, 1998*, edited by P. H. Mokler, F. Bosch, Th. Stöhlker, and A. Wolf [Phys. Scr. **T80** 52, (1999)], p. 209.
[6] U. Thumm *et al.*, Phys. Rev. A **56**, 4799 (1997).
[7] N. Selberg, A. Bárány, C. Biedermann, C. J. Setterlind, and H. Cederquist, Phys. Rev. A **53**, 874 (1996).
[8] U. Thumm, J. Phys. B **27**, 3515 (1994); **28**, 91 (1995).
[9] A. A. Scheidemann, V. V. Kresin, and W. D. Knight, Phys. Rev. A **49**, R4293 (1994).
[10] E. Sohmen, J. Fink, and W. Krätschmer, Z. Phys. B: Condens. Matter **86**, 87 (1992).
[11] S. Matt *et al.*, Z. Phys. D: At., Mol. Clusters **40**, 389 (1997).
[12] J. U. Andersen *et al.*, Phys. Rev. Lett. **77**, 3991 (1996).
[13] A. Bárány and C. J. Setterlind, Nucl. Instrum. Methods Phys. Res. B **98**, 184 (1995).
[14] A. Bárány in *Proceedings of the XX International Conference on Photonic, Electronic, and Atomic Collisions*, edited by Friedrich Aumayr and Hanspeter Winter (World Scientific, Singapore 1998).
[15] H. Shen *et al.*, Phys. Rev. A **52**, 3847 (1995).
[16] S. Petrie, J. Wang, and D. K. Bohme, Chem. Phys. Lett. **204**, 473 (1993).
[17] D. B. Cameron and J. H. Parks, Chem. Phys. Lett. **272**, 18 (1997).
[18] P. Scheier, B. Dünser, and T. D. Märk, Phys. Rev. Lett. **74**, 3368 (1995).
[19] E. E. B. Campbell, T. Raz, and R. D. Levine, Chem. Phys. Lett. **253**, 261 (1996).
[20] T. Schlathölter, O. Hadjar, R. Hoekstra, and R. Morgenstern, Phys. Rev. Lett. **82**, 73 (1999).
[21] J. Opitz, H. Lebius, B. Saint, S. Jacquet, B. A. Huber, and H. Cederquist, Phys. Rev. A **59**, 3562 (1999).
[22] J. Opitz *et al.* (unpublished).
[23] B. Walch *et al.*, Phys. Rev. A **58**, 1261 (1998).
[24] J. D. Jackson, *Classical Electrodynamics* (Wiley, New York, 1975).
[25] A. Bárány *et al.*, Nucl. Instrum. Methods Phys. Res. B **9**, 397 (1985).
[26] A. Arnau *et al.*, Surf. Sci. Rep. **27**, 113 (1997).
[27] H. Cederquist *et al.*, in *Proceedings from the IX International Conference of the Physics of Highly Charged Ions, Bensheim, Germany, 1998* (Ref. [5]).
[28] J. Burgdörfer, P. Lerner, and F. W. Meyer, Phys. Rev. A **44**, 5674 (1991).

[29] F. W. Meyer, L. Folkerts, H. O. Folkerts, and S. Schippers, Nucl. Instrum. Methods Phys. Res. B **98**, 441 (1995).
[30] J. Burgdörfer, in *Review of Fundamental Processes and Applications of Atoms and Ions*, edited by C. D. Lin (World Scientific, Singapore, 1993).
[31] G. Seifert, R. Gutierrez, and R. Schmidt, Phys. Lett. A **211**, 357 (1996).
[32] S. Matt *et al.*, Z. Phys. D: At., Mol. Clusters **40**, 389 (1997).
[33] T. Bastug *et al.*, Phys. Rev. B **55**, 5015 (1997).
[34] P. Hvelplund *et al.*, Nucl. Instrum. Methods Phys. Res. B **9**, 421 (1985).
[35] M. C. Larsen, P. Hvelplund, M. O. Larsson, and H. Shen, Eur. Phys. J. D **5**, 283 (1999).
[36] E. S. Parilis, Nucl. Instrum. Methods Phys. Res. B **88**, 21 (1994).
[37] O. B. Firsov, Zh. Éksp. Teor. Fiz. **36**, 1517 (1959) [Sov. Phys. JETP **9**, 1076 (1959).
[38] G. Moliere, Z. Naturforsch. **2a**, 133 (1947).
[39] S. Winecki, M. P. Stöckli, and C. L. Cocke, Phys. Rev. A **55**, 4310 (1997).
[40] M. O. Larsson *et al.*, Int. J. Mass Spectrom. Ion Processes **177**, 51 (1998).
[41] P. F. Coheur, M. Carleer, and R. Colin, J. Phys. B **29**, 4987 (1996).
[42] V. Piacente, G. Gigli, P. Scardala, A. Giustini, and D. Ferro, J. Phys. Chem. **99**, 14 052 (1995).
[43] C. K. Mathews *et al.*, J. Phys. Chem. **96**, 3566 (1992).
[44] J. Abrefah, D. R. Olander, M. Balooch, and W. J. Siekhaus, Appl. Phys. Lett. **60**, 1313 (1992).
[45] S. Martin, J. Bernard, L. Chen, A. Denis, and J. Désesquelles, Eur. Phys. J. D **4**, 1 (1998).
[46] N. Shima, T. Mikumo, and H. Tawara, At. Data Nucl. Data Tables **34**, 357 (1986).
[47] R. Ali, C. L. Cocke, M. L. A. Raphaelian, and M. P. Stöckli, Phys. Rev. A **49**, 3586 (1994).
[48] S. Winecki, M. P. Stöckli, and C. L. Cocke, Phys. Rev. A **56**, 538 (1997).
[49] W. C. Turkenburg, B. G. Colenbrander, H. H. Kersten, and F. W. Saris, Surf. Sci. **47**, 272 (1975).
[50] P. Hvelplund *et al.*, Phys. Rev. Lett. **69**, 1915 (1992).
[51] Y. Nakai *et al.*, J. Phys. B **30**, 3049 (1997).
[52] T. Schlathölter, R. Hoekstra, and R. Morgernstern, J. Phys. B **31**, 1321 (1998).
[53] S. Hunsche *et al.*, Phys. Rev. Lett. **77**, 1966 (1996).
[54] R. Ehlich, O. Knospe, and R. Schmidt, J. Phys. B **30**, 5429 (1997).